WILEY-VCH

DOI: 10.1002/adma.201704477
Article type: Research News

The Self-Assembly of Cellulose Nanocrystals: Hierarchical Design of Visual Appearance

Richard M. Parker, Giulia Guidetti, Cyan A. Williams, Tianheng Zhao, Aurimas Narkevicius, Silvia Vignolini and Bruno Frka-Petesic*

Department of Chemistry, University of Cambridge, Lensfield Road, Cambridge CB2 1EW, UK

E-mail: sv319@cam.ac.uk

Keywords: cellulose nanocrystals, colloids, liquid crystals, self-assembly, structural color

Abstract. By controlling the interaction of biological building blocks at the nanoscale, natural photonic nanostructures have been optimized *via* evolution to produce intense coloration. Inspired by such biological nanostructures, the possibility to design the visual appearance of a material by guiding the hierarchical self-assembly of its constituent components, ideally using natural materials, is an attractive route for rationally-designed, sustainable manufacturing. Within the large variety of biological building blocks, cellulose nanocrystals are one of the most promising bio-sourced materials, primarily for their abundance, biocompatibility and ability to readily organize into photonic structures. Here, we review the mechanisms underlying the formation of iridescent, vividly-colored materials from colloidal liquid crystal suspensions of cellulose nanocrystals and report recent advances in structural control over the hierarchical assembly process as a toolbox for the design of sophisticated optical materials.

1. Introduction

A common strategy to produce intense coloration in nature consists of arranging fibrillar structural polysaccharides into helicoidal nanostructures.[1–5] In plants, such architectures are composed of cellulose nanofibers and are responsible for the intense blue color found in many fruits and leaves.[6–11] Importantly, cellulose nanocrystals extracted from natural cellulose fibrils can spontaneously self-assemble at the nanoscale to produce similar architectures capable of reflecting light in the visible spectrum.[12] Nanocellulose-based optical materials are non-bleaching, bio-compatible,[13] biodegradable,[14] low-cost and scalable, and as such offer enormous potential to sustainably replace traditional, potentially hazardous, colorants used industrially for food, cosmetics, art, textiles, sensing and security labeling.[15,16] In this Research News article, we describe the liquid crystalline behavior of cellulose nanocrystals in suspension and provide an overview of the toolbox available to control their self-assembly into vivid, structurally-colored materials. Methods of controlling the optical appearance, both in terms of color and angular response, are explained and expanded to consider the key role of geometrical confinement upon the self-assembly process. Finally, approaches to enhance cellulose nanocrystal-based optical materials are discussed in the context of extending their functional application.

2. Cellulose nanocrystals

Natural cellulose is produced in the plant cell wall in fibrillary form.[17] Generally, an individual cellulose fiber (diameter 5 – 20 μm) is formed from a bundle of nanofibrils (diameter 3 – 20 nm). The nanofibrils are made of elongated single crystalline domains separated periodically by more disordered regions.[18] The crystalline regions can be isolated by acid hydrolysis of the less ordered regions to give rigid rod-like nanoscale particles, commonly known as cellulose nanocrystals (CNCs), see **Figure 1b**.[19] To date, CNCs have

been extracted from a large variety of natural sources, spanning plants,[19] bacteria,[20] and tunicates.[21,22]

The most established methods of isolating colloidally stable CNCs are by strong sulfuric acid hydrolysis,[23,24] or hydrochloric acid hydrolysis[25] followed by TEMPO oxidation.[26,27] These methods yield inherently polydisperse suspensions of negatively-charged particles,[28] surface-functionalized with $–OSO_3^{(–)}$ or $–COO^{(–)}$ groups respectively. Hydrolysis conditions such as duration, reagent concentration and temperature, as well as the cellulose source, not only influence the yield of the process, but also highly affect the morphology, aspect ratio, polydispersity, degree of crystallinity and the surface charge of individual CNCs.[29–31] Importantly, as the colloidal stability of the CNCs is a prerequisite for any self-assembly to occur, insufficiently charged CNCs (such as isolated after hydrolysis by phosphoric acid[32] or hydrochloric acid[25]) do not lead to the same ability to self-assemble. Once prepared, the suspensions are purified by aqueous dialysis before further use in polar solvents,[33,34] however the use of either a surfactant[35,36] or additional surface functionalization[37–39] extends their stability range to extreme conditions or apolar solvents.

The properties of CNC are strongly related to their biological source and the extraction conditions.[40] Their surface properties and crystallinity index can therefore vary between 55 – 95%.[40–42] Typically, CNCs extracted from cotton and wood pulp consist of a few laterally-bound crystallites, with lengths varying between 100 – 350 nm, widths about 10 – 20 nm and thicknesses usually about 3 – 5 nm,[31,42] whereas those extracted from tunicate are much longer (up to a few microns) and form less bundles.[31,43] CNCs are built from a regular assembly of chiral D-glucose and as such retain some degree of chirality, as supported by recent observations and simulations indicating a twist in both their internal structure and their outer morphology, either on the individual crystallite level or on the formed bundles.[31,42,44–48]

CNCs also exhibit excellent mechanical properties, with the axial tensile modulus reported to be >130 GPa,[49,50] making them suitable for reinforcing polymer composites.[51] Finally, cellulose nanocrystals have birefringent optical properties that can be transmitted to the materials in which they are arranged, making them an outstanding material for photonic applications. The crystalline cellulose that composes the CNCs is intrinsically birefringent along the chain axis, with a reported birefringence of $n_e^{cell} = 1.618$ and $n_o^{cell} = 1.544$ for idealized cellulose fibers at 589.3 nm,[52] or as measured experimentally as $n_e^{cell} = 1.603$ and $n_o^{cell} = 1.523$ for ramie crystalline fragments in index-matched liquids.[53] However, the intrinsic birefringence, together with the high aspect ratio of CNCs and the optical index of the surrounding media, leads to the emergence of an extrinsic birefringence for individual CNCs relative to their long axis.[54] Collectively, the arrangement of such CNCs, in terms of packing and degrees of alignment, will either cancel out in the isotropic phase or lead, in the anisotropic phase, to the emergence of a local birefringence.[54–58]

3. Self-assembly from suspension to the solid state

The colloidal stability of the CNC suspension and its ability to self-organize into a liquid crystal are governed by the balance between orientation-dependent attractive and repulsive interactions. Attractive interactions are due to van der Waals forces, while the repulsive interactions encompass both short-range hard rod steric repulsions and longer-range repulsions of either steric or electrostatic nature, as described in essence by DLVO theory.[59,60] In polar solvents, such as water, the long-range repulsion is governed by the CNC surface charge and scales with the Debye-Hückel length, κ^{-1}, which strongly depends on the ionic strength I of the medium ($\kappa^{-1}(\mathrm{nm}) = 0.304/\sqrt{I(\mathrm{M})}$, in water at 25 °C) and greatly influences CNC self-organization.[61,62] Other methods of stabilization include the use of steric repulsion by polymer grafting[39,63–66] or the reduction of van der Waals forces in a refractive

index-matched, apolar solvent.[35,67] The dominance of these long-range interactions results in the nanorods interacting approximately as purely steric objects, with an effective volume and aspect ratio. Consequently, two extreme cases arise at the limits of electrolyte concentration. At the lower limit, the electrostatic repulsions are dominant and very long-range, promoting kinetic arrest, even at low CNC concentration (*ca.* 1 wt.%.); this is generally referred to as a repulsive Wigner glass,[68–70] but for sufficiently long aspect ratios (e.g. bacterially-derived CNC) it can slowly evolve into a nematic phase (e.g. after a week, for $I < 10$ μM).[46] At the upper limit, which strongly depends on the counter-ion valence,[71] the colloidal stability is disrupted and leads to either a slow evolution into an attractive colloidal gel,[69,70,72] or to flocculation and sedimentation.[59] Notably, the use of insufficiently charged CNCs results in similar behavior.[32,73]

Colloidal CNC suspensions can spontaneously exhibit lyotropic liquid crystalline behavior. The emergence of this alignment arises from a trade-off between the rotational and translational entropies of individual nanorods, as demonstrated by Onsager in a seminal work,[74] and later refined to account for lower aspect ratios,[75,76] polydispersity[77,78] and electrostatic effects.[61,79,80] While low CNC concentrations permit a random orientation of the nanorods resulting in an isotropic phase, higher concentrations favor local mutual alignment between individual nanorods. In practice, it is observed that the sample undergoes a first order phase transition from an isotropic to a cholesteric phase upon increasing concentration, with a coexistence of both phases in the intermediate regime. The cholesteric order, also often referred to as chiral nematic, is characterized by a local orientation of the nanorods along a common direction, defined as the director **n**, that spatially rotates in a helicoidal structure about an axis, **m**. In the case of CNCs, the helix is found to be always left-handed and is attributed to the chirality of the interaction between the nanorods, however the underlying mechanism is still under debate.[45–48,81] The distance along the helical axis that separates

nanorods of the same orientation after a 360° rotation is commonly defined as the cholesteric pitch, p. This ordered phase inherits the birefringence of the aligned nanorods and is easily identified in polarized optical microscopy by its characteristic cholesteric fingerprint pattern (**Figure 1c**).[33] An example diagram capturing the phase behavior of a CNC suspension is illustrated in **Figure 1a**.

The interaction of light with a birefringent cholesteric phase leads to optical phenomena that strongly depend on the cholesteric pitch of the suspension, as well as the wavelength, polarization and propagation direction of the incident light.[82] The continuous rotation of **n** along which the birefringent nanorods align creates a helicoidal variation of the refractive index along **m**. The propagation of light at directions normal to **m** is responsible for the observation of the fingerprint pattern between crossed polarizers (**Figure 1c**). The periodicity of this pattern corresponds to half of the cholesteric pitch and is typically in the micron range for both aqueous[33] and organic suspensions.[34,35] When light propagates along the **m** axis, it is observed that such spatial modulation of the refractive index leads to the reflection of strongly circularly polarized light for a certain interval of wavelengths, as described by both analytical[83–86] and numerical[87–89] approaches. The peak reflected wavelength is given to a good approximation by:[82,90]

$$\lambda = n_{av}\, p \cos \varphi \tag{1}$$

where $n_{av} = (n_e + n_o)/2$ and describes the local average refractive index of the extraordinary and ordinary optical indices in the phase, n_e and n_o respectively, p is the pitch of the helicoid and φ is the angle of incident light with respect to **m** inside the suspension.[58,91,92] Such reflection occurs for a specific interval of wavelengths, which is defined in first approximation by the refractive index contrast $n_o p < \lambda < n_e p$. By convention, the handedness of the reflected circular polarized light is the same as the helicoidal structure, i.e. left-circular polarized light for CNCs.[83–85,93] However, as noted above, the pitch in CNC

suspensions are typically in the micron range and thus do not allow for the reflection of visible light. However, visible light can still be diffracted in transmission (often producing higher harmonics) by cholesteric domains oriented nearly perpendicular to the incident light. This allows for accurate determination of the average pitch across the sample, following **Equation 1**.[58,91,92]

A key aspect of cholesteric colloidal liquid crystals is their ability to retain their helicoidal arrangement after removal of solvent (**Figure 1d,e**).[94,95] This property enables a cholesteric suspension of CNCs to be used as a chiral template to produce solid-state hierarchical materials with unique optical properties. This is typically achieved by evaporation-induced self-assembly, whereby a CNC suspension is evaporated under controlled conditions to give a solid film. However, a novel approach based on vacuum-assisted self-assembly has been recently reported,[96] whereby vacuum membrane filtration of the CNC suspension was able to produce a filtration cake with a well-ordered helicoidal order, with the pitch shown to be adjustable *via* the pressure differential.

To produce precisely-structured solid-state films, it is imperative to have control over the liquid crystalline order across each stage of drying: from an initial isotropic suspension to a fully cholesteric phase and finally to the solid state, *via* a kinetically-arrested gel. Consequently, many inter-related parameters strongly influence the final film properties.[97] Notably, while the evaporation rate for a drying suspension is typically constant for a given experiment, the corresponding concentration increase is non-linear and as such, the time interval available for cholesteric formation is highly dependent on the initial suspension conditions. For example, an initially dilute suspension (e.g. 1-2 wt%) will typically spend most of its ‘drying time’ in the isotropic phase, significantly reducing the time allocated after the phase transition for self-assembly to occur.[98]

When an isotropic CNC suspension is gradually concentrated through loss of solvent, it first undergoes the phase transition described in **Figure 1a**. During this transition the nanorods assemble *via* a nucleation-and-growth process into small anisotropic droplets of higher local concentration, referred to as *tactoids,* that then slowly coalesce and/or sediment.[33,56,61,99,100] Upon further concentration these randomly-oriented tactoids merge into a polydomain mesophase, trapping defects and disclinations at domain boundaries. Notably, for nanorods of larger aspect ratios (e.g. Avicel or tunicate), the activation energy to form tactoids vanishes and as a result, their phase transition instead follows a different pathway, *via* a slow spinodal decomposition.[101] In this case, the unstable isotropic phase develops homogeneous density fluctuations that progressively phase-separate into interpenetrated isotropic and anisotropic phases, the latter eventually coalescing and sedimenting if given enough time, as reported for other rod-like colloidal systems.[102,103] Regardless of the phase transition mechanism, when allowed sufficient time the cholesteric phase can relax and reduce the defect content, giving rise to larger domains of uniform orientation. In this regime, the pitch continues to decrease with increasing concentration to maintain its thermodynamic equilibrium.

As the cholesteric phase concentrates further, the suspension crosses a point of kinetic arrest prior to reaching the solid-state. This kinetic arrest occurs when the closely-packed nanorods become sufficiently restricted in their ability to relax and rearrange their mutual position and orientation, potentially facilitated by the build-up of ionic strength upon concentration increase.[72,104] From this point onwards, evaporation of the remaining solvent will induce a mechanical constraint on the formed gel, with the macroscopic geometry becoming crucial upon the preservation of the cholesteric ordering in the solid-state. For example, when a CNC suspension is dried in a Petri dish, evaporation after the point of kinetic arrest leads to a quasi-unidirectional compression of the cholesteric structure along the vertical axis. This induces an

anisotropic contraction of the cholesteric pitches that distorts the domains differently depending on their orientation. The cholesteric phase in suspension is translated into a helicoidal nano-architecture in the resultant film, as confirmed by the characteristic Bouligand arches[1] observed in cross-section by electron microscopy (**Figure 1e**).[33,105] Most significantly, while the pitch is micron-sized in the cholesteric suspension, it reaches the sub-micron range in the solid film (**Figure 1e**). This is important for optical applications, as this decrease in the pitch can shift the optical reflection band into the visible, enabling vivid structural color in reflection (**Figure 1d**).[95,100,106] The optical response of such films still locally obey the angular dependence described in **Equation 1**, but correction for Snell's law is necessary to allow for the film-air interface, as described by Fergason's law (**Figure 2a**).[88,107–109]

As discussed above, the composition of the initial CNC suspension alone is often not enough to define the final appearance of the film, with consideration of the conditions and geometry during drying also required. Furthermore, such parameters can have different effects at different stages of the drying process or can interact to give unexpected results. The following sections review the current methods to design the appearance of an optical film from the initial CNC suspension, which for clarity are addressed separately, as follows: (i) controlling the cholesteric pitch, (ii) controlling the alignment of the mesophase and (iii) the role of geometry.

4. Controlling the pitch

The optical properties of CNC-based materials are intrinsically linked to the pitch, which is determined by both the initial CNC suspension and its evolution during drying. Furthermore, the pitch can be influenced by different mechanisms at various points in the drying process.

For instance, the addition of a non-volatile additive or co-solvent, may influence the equilibrium pitch of the cholesteric suspension (e.g. D-glucose leads to a blue-shift),[106] but will always hinder the complete collapse of the film, leading to a red-shift,[94,106,110–112] The following section discusses methods to influence the pitch in suspension or during the drying process to produce a film of a specific color, as summarized in **Table 1**.

Table 1. Summary of the different mechanisms that influence the cholesteric pitch of sulfated-CNCs, either in the initial suspension or during the evaporation process.

	Mechanism	Technique	Decreasing the pitch (i.e. blue-shift)	Increasing the pitch (i.e. red-shift)
Initial suspension	Controlling CNC shape	Fractionation (e.g. centrifuge, phase transition)	Shorter rods	Longer rods
	Breaking aggregates	Tip sonication	N/A	Time/energy input
	Repulsive interactions	Screening charge	Adding electrolyte (e.g. salt, acid)	Removing electrolyte (e.g. dialysis)
		Decreasing surface charge	Heating (desulfation)	N/A
	Attractive interactions	Solvent exchange	Higher ε_r solvent	N/A
Evaporation process	Self-assembly conditions	Duration of the self-assembly	Lower RH	Higher RH
			Higher temperature	Lower temperature
			Low initial concentration	High initial concentration
			Low initial volume	High initial volume
	Mechanics	Reduce unidirectional collapse	N/A	Non-volatile additive
		Deformation	Compression	Swelling
		Helix alignment	Vertical	Tilted

Decreasing the range and/or the strength of the electrostatic repulsions between nanorods, either by addition of electrolyte or reduction of the CNC surface charge, is known to strongly decrease both the pitch and the proportion of cholesteric phase in the suspension.[45,46,61,94,97] This is understood as a contraction in the Debye-Hückel length, which reduces the effective

nanorod volume and results in closer packing with a stronger chiral interaction.[45,46] Peculiarly, aqueous suspensions of Jeffamine-grafted CNCs display the opposite trend, namely a pitch increase upon addition of salt.[66] Furthermore, excessive salt can partially aggregate CNCs and could explain unusual pitch trends.[15,113] While the nature of common inorganic cations (e.g. H^+, Na^+, K^+) does not affect the phase transition and the pitch,[61] it has been reported that bulky cations favor a larger pitch in suspension,[114] while conversely smaller pitches have been obtained by using polyvalent ions.[115] Finally, the surface charge can be reduced at acidic pH for carboxylated-CNCs (protonation), or in conjunction with e.g. heating for sulfated-CNCs (desulfation).[73,116] In the latter case, the pitch decrease is observed even after removal of the released sulfuric acid.[94,114]

The exchange of water (ε_r = 80 at 20 °C) for a solvent with a higher dielectric permittivity, such as formamide (ε_r = 111) or N-methylformamide (ε_r = 189), results in significantly smaller pitches in suspension.[34] Solvent exchange can be achieved without an intermediate drying step *via* distillation, ensuring that CNC aggregation is not introduced. Higher permittivity suspensions have been reported to reduce the viscosity-normalized self-organization time, the dependence of the equilibrium pitch on the CNC concentration and the final equilibrium value of the pitch. While the precise mechanism behind these observations is not yet clear, higher permittivity solvents are expected to increase the effective charge of the nanorods and the κ^{-1} length, while at the same time affecting both attractive van der Waals interactions and the hydrogen bond network between CNCs.

The length and aspect ratio of the nanorods affect the cholesteric pitch, with longer nanorods leading to a larger pitch in the produced film.[94,95] This has been observed for CNCs extracted from cotton and wood pulp by exploiting the aspect ratio dependence of the phase transition to isolate nanorods of different lengths, as longer rods transit into the cholesteric phase first.

This trend is in qualitative agreement with simulations of the self-organization of slightly helicoidal nanorods.[117,118]

Tip sonication is routinely used in the preparation of CNC suspensions to favor their dispersion, however the cholesteric pitch is also observed to increase with the energy input.[119] While the measured conductivity rise suggested a release of trapped ions, this alone cannot explain this pitch increase. Instead, we hypothesize that pre-existing CNC aggregates act as chiral dopants, enhancing the cholesteric twist, and their destruction by tip sonication causes the observed red-shift, as well as the observed turbidity decrease.

Fast evaporation of an isotropic suspension leads to polydomain films with a smaller pitch.[97,100] The polydomain structure arises from the insufficient time allowed for the nucleated tactoids to merge, creating grain boundaries between domains. Since the nanorods cannot pack as efficiently in the grain boundaries, they experience closer packing inside the cholesteric domains,[120] which is expected to decrease the pitch.[91]

Thermal effects have been shown to have negligible effect on the equilibrium pitch in a sealed suspension,[114] unless desulfation occurs. Evaporating an initially isotropic suspension at higher temperatures leads to significantly higher drying rates and thus decreases the pitch in the film.[97] However, a temperature increase applied during the kinetically-arrested regime has been reported to red-shift the produced film, allowing for localized colors or patterns.[121]

5. Controlling the alignment

Alignment can be considered across hierarchical length scales: from the relative position of discrete nanorods (*nanoscale*), through the orientation of tactoids in suspension (*microscale*),

to the long-range coherence of the director and helical axis within the cholesteric phase (*macroscale*). In stark contrast to the cholesteric pitch, the importance of alignment in nanostructured CNC-based materials has only recently been appreciated. The following section describes methods to control the alignment in the suspension and how this correlates to the optical appearance in the solid-state.

The simplest example of control over the alignment is anchoring – the process by which an interface can favor specific liquid crystal orientations. In the CNC suspension, anchoring at the interface between the isotropic and the anisotropic phase is negligible and enables all possible orientations of the nanorods. This allows for the formation of cholesteric tactoids with unperturbed cholesteric order.[33,35,99] However, at a smooth, impenetrable surface (e.g. a solid substrate or an immiscible liquid), the nanorods adopt planar anchoring, whereby the director lies in any direction parallel to the interface (**Figure 2b**).[58,99] In turn, this induces an anchoring of the helical axis normal to the interface, which then propagates further into the suspension.

Alignment can be induced by applying hydrodynamic shear to a CNC suspension (**Figure 2c**).[45,55,122–129] In the isotropic phase, the average orientation of nanorods under low shear (0.5 s^{-1}) is normal to the shear plane, while at high shear (500 s^{-1}) it is parallel to the shear direction.[123] In the cholesteric phase, high shear disrupts the helicoidal order and leads to parallel alignment.[45] Solid birefringent materials with nematic order can thus be produced by applying shear continuously during the evaporation process,[122,126] or during fast deposition by either spin-coating[55,127] or blade-coating.[124,125,127–130] More importantly, applying moderate hydrodynamic shear to a drying suspension can lead to helicoidal nanostructures with uniform vertical alignment of the helical axis, as observed near the center of a suspension dried on a circularly oscillating plate.[98,131]

External electric and magnetic fields lead to a strong orientational coupling with individual CNCs and can be used to control the overall alignment, both in aqueous or apolar suspension. For a dilute CNC suspension, electric fields induce parallel alignment of CNCs,[132,133] due to both permanent and induced electric dipoles,[134] enabling its use as an electro-optical spatial light modulator.[134,135] Applied to the cholesteric phase, moderate AC fields (100 – 300 V/cm) initially orient the helical axis **m** normal to the field, while stronger fields progressively unwind the cholesteric phase (**Figure 2e**).[92] Since the cholesteric periodicity causes strong iridescence when observed in transmission, the observed colors can be dynamically tuned with the electric field, until a fully paranematic phase forms parallel to the field. Unlike shear and electric fields, magnetic fields locally induce a perpendicular alignment of CNC nanorods, due to their negative diamagnetic susceptibility.[54,136] For this reason, they stabilize and orient the cholesteric order into a macroscopic monodomain with **m** parallel to the field (**Figure 2d**).[45,114,120,137–141] In contrast, rotating magnetic fields (e.g. 10 rpm) were shown to favor parallel orientation of the nanorods,[141] and thus untwist the cholesteric phase to favor a nematic order normal to the field (**Figure 2e**).[138–140] Solid materials retaining magnetically-aligned helicoidal structures have been successfully prepared by either trapping the cholesteric phase by solvent photopolymerization[139,140] or by further drying the suspension into a solid film.[97,109,139,142] Recently, the use of moderate magnetic fields (e.g. 0.5 – 1.2 T) has been shown to successfully induce alignment in the cholesteric phase.[120,138] Significantly, by arranging commercial neodymium magnets in the immediate vicinity of the drying suspension, the precise direction of **m** can be can controlled in the produced film (**Figure 4a**).[109] This allows for either reduced off-specular reflection (for a vertical field), enhancement of the off-specular photonic response with a controlled directionality, or even a simple route to patterned films by using more complex magnet geometries.

The application of mechanical stress to the cholesteric phase, as present in a kinetically-arrested suspension, is critical for both the pitch and the alignment of the final nanostructure. For example, the vertical compression imposed in the center of a suspension drying in a dish induces a flattening of the domains (**Figure 2f**). For tilted domains, such compression causes both a deviation of their helical axes towards the direction of compression, as well as less efficient pitch compression in comparison to the well-aligned domains. This explains the peculiar red-shift observed in off-specular conditions with polydomain films, resulting in a 'pixelated' appearance.[108,109] Similarly, mechanical compression of a composite film (e.g. co-assembled with a resin) causes a blue-shift (**Figure 4b**).[112] Reciprocally, applying tensile load favors alignment of the nanorods in the direction of the induced stretch.[143] This is observed close to the edge of the dish (**Figure 1d**), where wetting of the kinetically-arrested suspension on the sidewalls during the final stages of drying induces a radial strain, causing both birefringence and decreased pitch. This effect often occurs in concert with a degree of shear-induced red-shift and can give rise to complex edge effects;[100] this is not to be confused with the coffee-ring effect, as discussed later. Interestingly, a thin film with a chess-board pattern with parabolic focal conics has been reported,[144] as expected from the lateral buckling of a well-aligned cholesteric monodomain when the pitch shrinks faster than the thickness contraction.[101] Buckling of the helicoidal structure is typically observed when compression is applied normal to the helical axis, as reported for both extremely tilted domains in magnetically-aligned films,[109] and in radially-aligned microparticles.[58] Finally, the compression of a concentrated disorganized phase (e.g. a sheared gel) produces transparent films with strongly disordered cholesteric features, enabling its use as an optical depolarization filter.[145]

6. The role of geometry

The geometry of a drying suspension strongly determines both the macroscopic shape of the produced solid material as well as its nanoscale structure. It controls the anchoring and the complex dynamics of drying (gradient of concentration, surface tension, wetting, evaporation front, capillary forces, etc.), but it also plays a key role in the mechanical compression once the kinetic arrest has occurred. Moving beyond the simple case of drying a suspension in a dish, this section will discuss three notable examples of geometrical confinement: thin films, sessile drops and spherical droplets.

The simplest example of geometrical confinement is the production of thin films (<5 µm), as reported for the evaporation of a small volume of suspension in a Petri dish.[88] While the thickness of such films is only an order of magnitude larger than the pitch length, this is still sufficient to produce vibrant structural colors.[87] In such thin-film confinement, a planar orientation of the cholesteric nanostructure is easily obtained, even under fast drying conditions, where disclinations in the cholesteric order are likely to be trapped.[146] In the case of extremely thin films (only 1-2 µm), the discrete change of pitch forced by these disclinations becomes significant and can lead to a mosaic of distinct colors (**Figure 3a**).[56]

The evaporation of a CNC suspension confined within a sessile drop introduces additional complexity to the self-assembly of colored films.[147] In this geometry, the dynamics of the contact line and its pinning to the substrate play an essential role in the produced film. Initially, in the absence of a container, the suspension can spread across the substrate and reach an equilibrium shape. This stage is governed by the balance of capillary and gravity forces and can be modified by both surface tension and surface chemistry.[148] These wetting conditions constrain the maximum height of the drop and thus the volume of suspension per surface area. At the edge, the decrease in height scales laterally with the capillary length (~2.7

mm for water) and leads to either a small curved sessile drop or a larger flat puddle, depending on the volume of suspension.[148]

As the solvent evaporates, the competition between the volume decrease and the emergence of mass flows has opposite effects on the contact line displacement and leads to a variety of scenarios that strongly affect CNC deposition. On untreated glass or acrylic substrates, the higher evaporation rate near the edge generates an outward radial capillary flow inside the drop. This causes accumulation of nanorods at the edge and pinning of the contact line, resulting in a ring-shaped deposit often referred to as a coffee ring stain (**Figure 3b**).[106,149] This radial flow also induces shear alignment that can disrupt the cholesteric order and cause linear birefringence. The reduction of such flow can be achieved by increasing the viscosity with a thickener[150] (e.g. glucose,[149] which also causes the aforementioned red-shift[106]), as demonstrated in **Figure 3b**. Alternatively, a Marangoni counter-flow can be favored using two solvents of different volatility and surface tension, as reported recently using an ethanol-enriched atmosphere; however such disturbances lead to a polydomain texture and birefringent edges.[151] Recently, the preference of particle-interface over particle-particle interactions has been shown to be key in suppressing the coffee-ring effect in many colloidal systems;[152–154] increasing the affinity of the nanorods for the surface can be achieved using hydrophilic substrates (e.g. glass cleaned by oxygen plasma or with strong acid or base), with the produced films showing more uniform deposition in the meniscus region with minimal accumulation at the edge.[155] Incidentally, CNC suspensions cast at low pH on untreated glass surfaces leads to a similar result and usually produce a film that is strongly attached to the substrate. This CNC surface coverage can reduce the pinning of the contact line and explains the peculiar stick-slip behavior that leads to concentric cracks and an uneven height profile in the final film.[156] Finally, a binary mixture of water and propylene glycol has been shown to

suppress pinning in sessile drops,[157] and this has been applied to suppress the stick-slip pattern in CNC films.[156]

The confinement of a cholesteric phase within a spherical droplet provides an idealized geometry for self-assembly, where the high curvature and the absence of a contact line leads to a very different architecture.[146] Emulsions of cholesteric CNC microdroplets in an immiscible oil have been recently reported using a microfluidic flow-focusing device.[58,158] For droplets with radius <115 µm, the planar anchoring at the liquid-liquid interface enables the cholesteric phase to assemble into a monodomain Frank-Pryce architecture,[159–161] recognizable between crossed polarizers as a concentric fingerprint pattern superimposed with a Maltese cross (**Figure 3c:center**). Interestingly, the topological defect in the droplet center leads to an isotropic core. Moreover, planar anchoring over the whole droplet surface generates radial disclinations that connect the central core to the droplet surface.[161] The lyotropic nature of the cholesteric phase explains the lower local density in the defect regions, which can be successfully used to accommodate a variety of nanoparticles of ~200 nm in diameter in the isotropic center or in periodic arrays along the radial disclinations (**Figure 3c:right**).[158,162] For smaller droplets (radius < 40 µm), the isotropic core is instead replaced by a central tactoid, surrounded by a thin Frank-Pryce shell (**Figure 3c:left**). Finally, microparticles with such cholesteric structures have been obtained by exploiting photopolymerization of polyacrylamide precursors.[163,164]

The self-assembly of CNCs within a spherical geometry is both a useful tool to understand the mechanisms involved, as well as a route to prepare hierarchically-structured microparticles. The progressive loss of solvent from a dilute CNC droplet results in an *in situ* phase transition and self-organization into a Frank-Pryce cholesteric architecture, which upon further drying leads to a nanostructured microparticle (**Figure 3d**).[58] The cholesteric phase nucleates and

grows inwards from the interface, incorporating any tactoids that may be initially present. Observation of the shrinking microdroplet allows for monitoring of the evolution of the pitch as a function of concentration over a much wider range. In such a pitch evolution diagram, as exemplified in **Figure 3e**, the pitch at low concentration matches well with the bulk suspension (as measured in thin capillaries) and follows a power law of approximately $p \propto c^{-1}$. Above a specific concentration c_g, attributed to kinetic arrest,[58,165] the pitch scales further as $p \propto c^{-1/3}$. This behavior is expected when the additional pitch decrease is due to the three-dimensional compression specific to a contracting sphere, as opposed to the one-dimensional compression in the standard film geometry. Such a clear transition in the continuous evolution of the pitch enables c_g to be precisely measured. Complete drying of the microdroplet leads to a microparticle that retains the radially-aligned helicoidal nanostructure (**Figure 3d**). The final pitch is significantly larger than in films cast from the same suspension, thus shifting the optical bandgap to the infrared, and illustrates the importance of geometry on the control of the final nanostructure. Moreover, the orthoradial component of the compression leads to significant buckling of the final microparticle, as noted previously.

7. Building functional materials

Optical materials prepared from cellulose nanocrystals suffer from several limitations (e.g. brittleness) that limit their wider adoption. By utilizing co-assembly, post-processing or lamination, CNC-based photonic materials can be prepared to overcome such shortcomings while also offering additional functionality.

The co-assembly of CNCs with weakly interacting additives significantly reduces the brittleness of the produced films while preserving the formation of the helicoidal nanostructure and causing a red-shift of the optical bandgap (**Figure 4e**). This has been

demonstrated with zwitterionic surfactants,[166] neutral or anionic polymers,[111,167–169] amino resins or sol-gel precursors,[110,112] and cross-linked latex nanoparticles.[170] The cholesteric arrangement of CNCs can also accommodate small nanoparticles without disruption of the phase,[171–176] e.g. plasmonic gold nanorods, allowing for complex chiroptical effects.[172,173]

The post-processing of CNC films can be required to stabilize the structure for further applications. Redispersion of CNC films upon immersion in water can be prevented by desulfation of the dry material by applying either vacuum[177] or heat to the protonated CNC form,[73,94] or by immersion in strong base.[178] Exploiting desulfation and the natural brittleness of CNC films, mechanical grinding has been shown to give water-resistant flakes with structural pigmentation.[177] Finally, prolonged immersion of a film in strong base at elevated temperature leads to partial dissolution of the nanorods, resulting in a blue-shift and dramatic improvement of the mechanical properties.[178]

Notably, the combination of CNC co-assembly with silica sol-gel precursors and its post-processing by pyrolysis allows for the templating of chiral mesoporous glass that displays the chiroptical properties of CNC films, but with an improved flexibility and enhanced functionalities such as solvent or pressure sensing.[110,179] Similarly, a chiral mesoporous resin with modifiable swelling properties has been obtained by co-assembly with a resin precursor, followed by selective removal of the CNC template with strong base (**Figure 4c**).[180]

The integration of CNC films into larger laminar constructs has been explored to develop expanded mechanical or optical properties. Thin, sandwiched structures have been obtained by embedding a CNC film within a polymer,[181] resulting in both intense structural coloration, enhanced mechanical properties and a shape memory effect. Relatedly, depositing CNC films onto each face of a birefringent membrane (that itself acts as a half-wave

retardance plate), enables simultaneous reflectance of both left and right-circularly polarized light, mimicking the reflection of the jewel beetle *Chrysina resplendens* (i.e. exceeding 50% reflectance, as shown in **Figure 4d**).[182] The same optical mechanism has been exploited by impregnating micrometer-scale planar gaps in CNC films with a nematic liquid crystal, forming a similar birefringent layer that could be actuated with temperature or electric fields to switch the reflected spectrum and its polarization state.[183]

8. Applications and overview

The versatility of naturally-derived CNC-based materials coupled to their biocompatibility offers a broad range of applications, from low-cost decoration to more sophisticated uses. In practice, grinding CNC films into flakes of various sizes allows for the production of edible structurally-colored glitter or powder for spray-coating that is suitable for food coloring, paints or cosmetics.[177] Beyond the aesthetic, the unique ability to reflect only a specific polarization of light at a precise wavelength band is beneficial for anti-counterfeiting applications (**Figure 4**). Such features can be further diversified by producing micro- and macroscale patterning (e.g. using temperature,[121] compression[112], swelling,[180,184] magnetic field orientation,[109] or *via* additional CNC-based depolarizing coatings[145]) or integration of optically active dopants such as up-converting or luminescent dyes[185] or nanoparticles.[175,176] Finally, since the underlying nanostructure defines the reflected color, a structural response (e.g. swelling) to an external stimulus allows for the design of cheap, biodegradable optical sensors. To date, CNC-based colorimetric sensors have been reported for humidity,[182,186–188] solvent[184,186] and mechanical pressure.[186]

In summary, we review the current understanding of the self-assembly mechanisms at play, and the available toolbox to control it across different length scales. We believe that the self-

assembly can be simplified into two regimes; a colloidal liquid crystal suspension, followed by a kinetically trapped gel. In the colloidal regime, the transition to a cholesteric phase, surface anchoring and the interaction with external fields are dictated by thermodynamics, while kinetics drives the nucleation and growth of the tactoids, their coalescence and defect dynamics. In the kinetically-arrested regime, the relaxation between nanorods becomes hindered and thermodynamics stops playing a role. Here, further evaporation of the remaining solvent causes the compression of the formed nanostructure in directions imposed by the drying geometry, and locally affects both the cholesteric orientation and its pitch. This final step, which brings the pitch into the sub-micron range, is critical for both the color and optical appearance (e.g. metallic *vs* matte) of the produced film.

Natural hierarchical nanostructures generally fulfill several functions at once (e.g. structural coloration, toughness, superhydrophobicity) and are the result of assembly processes, whose complexity in many biological systems is still beyond our understanding. To generate such sophisticated architectures, both natural and artificial assembly routes might benefit from multi-step treatments applied in a specific sequence, allowing the building up of complexity. For such constructs to emerge, thermodynamics leads only to reproducible static equilibrium states, while kinetics ensures by sequentially limiting or *locking in* specific degrees of freedom that the benefit of previous ordering processes is not lost. Gaining better understanding and control over kinetically constrained states is crucial, as this underexploited regime allows for fine manipulation of the final, truly multi-functional architectures. This concept has been explored so far with geometrically-confined systems, but it has much greater potential.

Acknowledgements

This work was supported by a BBSRC David Phillips Fellowship [BB/K014617/1], the EPSRC [1525292 and EP/L016087/1], the European Research Council [ERC-2014-STG

H2020 639088] and the Winton Programme for the Physics of Sustainability. B.F.-P. thanks Laurent Heux and Yu Ogawa for useful discussions.

Received: ((will be filled in by the editorial staff))
Revised: ((will be filled in by the editorial staff))
Published online: ((will be filled in by the editorial staff))

References

[1] Y. Bouligand, *Tissue Cell* **1972**, *4*, 189.

[2] B. D. Wilts, H. M. Whitney, B. J. Glover, U. Steiner, S. Vignolini, *Mater. Today Proc.* **2014**, *1*, 177.

[3] M. Mitov, *Soft Matter* **2017**, *13*, 4176.

[4] D. Lee, *Nature's Palette: The Science of Plant Color*, The University Of Chicago Press, Chicago, **2007**.

[5] O. Karthaus, *Biomimetics in Photonics*, CRC Press, **2012**.

[6] S. Vignolini, P. J. Rudall, A. V Rowland, A. Reed, E. Moyroud, R. B. Faden, J. J. Baumberg, B. J. Glover, U. Steiner, *Proc. Natl. Acad. Sci. U. S. A.* **2012**, *109*, 15712.

[7] S. Vignolini, E. Moyroud, B. J. Glover, U. Steiner, *J. R. Soc. Interface* **2013**, *10*, 20130394.

[8] R. M. Graham, D. W. Lee, K. Norstog, *Am. J. Bot.* **1993**, *80*, 198.

[9] G. Strout, S. D. Russell, D. P. Pulsifer, S. Erten, A. Lakhtakia, D. W. Lee, *Ann. Bot.* **2013**, *112*, 1141.

[10] D. W. Lee, *Nature* **1991**, *349*, 260.

[11] S. Vignolini, T. Gregory, M. Kolle, A. Lethbridge, E. Moyroud, U. Steiner, B. J. Glover, P. Vukusic, P. J. Rudall, *J. R. Soc. Interface* **2016**, *13*, 20160645.

[12] A. G. Dumanli, T. Savin, *Chem. Soc. Rev.* **2016**, *45*, 6698.

[13] S. Camarero-Espinosa, C. Endes, S. Mueller, A. Petri-Fink, B. Rothen-Rutishauser, C. Weder, M. Clift, E. Foster, *Fibers* **2016**, *4*, 21.

[14] G. Singh, C. Chandoha-Lee, W. Zhang, S. Renneckar, P. J. Vikesland, A. Pruden,

Water Res. **2016**, *104*, 137.

[15] J. P. F. Lagerwall, C. Schütz, M. Salajkova, J. Noh, J. Hyun Park, G. Scalia, L. Bergström, *NPG Asia Mater.* **2014**, *6*, e80.

[16] G. R. Meseck, A. S. Terpstra, M. J. MacLachlan, *Curr. Opin. Colloid Interface Sci.* **2017**, *29*, 9.

[17] B. B. Buchanan, W. Gruissem, R. L. Jones, *Biochemistry & Molecular Biology of Plants (2nd Edition)*, John Wiley And Sons, **2015**.

[18] Y. Nishiyama, U. J. Kim, D. Y. Kim, K. S. Katsumata, R. P. May, P. Langan, *Biomacromolecules* **2003**, *4*, 1013.

[19] B. G. Ranby, *Discuss. Faraday Soc.* **1951**, *11*, 158.

[20] A. J. Brown, *J. Chem. Soc., Trans.* **1886**, *49*, 432.

[21] B. G. Rånby, *Ark. För Kemi* **1952**, *4*, 241.

[22] P. S. Belton, S. F. Tanner, N. Cartier, H. Chanzy, *Macromolecules* **1989**, *22*, 1615.

[23] B. G. Rånby, *Acta Chem. Scand.* **1949**, *3*, 649.

[24] R. H. Marchessault, F. F. Morehead, N. M. Walter, *Nature* **1959**, *184*, 632.

[25] J. Araki, M. Wada, S. Kuga, T. Okano, *Langmuir* **2000**, *16*, 2413.

[26] S. Montanari, M. Roumani, L. Heux, M. R. Vignon, *Macromolecules* **2005**, *38*, 1665.

[27] A. Isogai, T. Saito, H. Fukuzumi, *Nanoscale* **2011**, *3*, 71.

[28] K. Fleming, D. G. Gray, S. Matthews, *Chemistry (Easton).* **2001**, *7*, 1831.

[29] X. M. Dong, J.-F. Revol, D. G. Gray, *Cellulose* **1998**, *5*, 19.

[30] W. Y. Hamad, T. Q. Hu, *Can. J. Chem. Eng.* **2010**, *88*, 392.

[31] S. Elazzouzi-Hafraoui, Y. Nishiyama, J.-L. Putaux, L. Heux, F. F. Dubreuil, C. Rochas, *Biomacromolecules* **2008**, *9*, 57.

[32] S. Camarero Espinosa, T. Kuhnt, E. J. Foster, C. Weder, *Biomacromolecules* **2013**, *14*, 1223.

[33] J. F. Revol, H. Bradford, J. Giasson, R. H. Marchessault, D. G. Gray, *Int. J. Biol.*

Macromol. **1992**, *14*, 170.

[34] J. R. Bruckner, A. Kuhnhold, C. Honorato-Rios, T. Schilling, J. P. F. Lagerwall, *Langmuir* **2016**, *32*, 9854.

[35] L. Heux, A. G. Chauve, C. Bonini, *Langmuir* **2000**, *16*, 8210.

[36] M. Salajková, L. A. Berglund, Q. Zhou, *J. Mater. Chem.* **2012**, *22*, 19798.

[37] J. Tang, J. Sisler, N. Grishkewich, K. C. Tam, *J. Colloid Interface Sci.* **2017**, *494*, 397.

[38] J. Natterodt, A. Petri-Fink, C. Weder, J. Zoppe, *Chim. Int. J. Chem.* **2017**, *71*, 376.

[39] F. Azzam, L. Heux, J.-L. Putaux, B. Jean, *Biomacromolecules* **2010**, *11*, 3652.

[40] M. S. Reid, M. Villalobos, E. D. Cranston, *Langmuir* **2017**, *33*, 1583.

[41] Y. Yue, C. Zhou, A. D. French, G. Xia, G. Han, Q. Wang, Q. Wu, *Cellulose* **2012**, *19*, 1173.

[42] W. P. Flauzino Neto, J.-L. Putaux, M. Mariano, Y. Ogawa, H. Otaguro, D. Pasquini, A. Dufresne, *RSC Adv.* **2016**, *6*, 76017.

[43] R. Tanaka, T. Kuribayashi, Y. Ogawa, T. Saito, A. Isogai, Y. Nishiyama, *Cellulose* **2017**, *24*, 3231.

[44] S. Hanley, J.-F. Revol, L. Godbout, D. Gray, *Cellulose* **1997**, *4*, 209.

[45] W. J. Orts, L. Godbout, R. H. Marchessault, J.-F. Revol, *Macromolecules* **1998**, *31*, 5717.

[46] J. Araki, S. Kuga, *Langmuir* **2001**, *17*, 4493.

[47] I. Usov, G. Nyström, J. Adamcik, S. Handschin, C. Schütz, A. Fall, L. Bergström, R. Mezzenga, *Nat. Commun.* **2015**, *6*, 7564.

[48] K. Conley, L. Godbout, M. A. Whitehead, T. G. M. Van De Ven, *Carbohydr. Polym.* **2016**, *135*, 285.

[49] A. Šturcová, G. R. Davies, S. J. Eichhorn, *Biomacromolecules* **2005**, *6*, 1055.

[50] F. L. Dri, L. G. Hector, R. J. Moon, P. D. Zavattieri, *Cellulose* **2013**, *20*, 2703.

[51] M. Mariano, N. El Kissi, A. Dufresne, *J. Polym. Sci. Part B Polym. Phys.* **2014**, *52*,

791.

[52] P. H. Hermans, *Contribution to the Physics of Cellulose Fibres: A Study of Sorption, Density, Refractive Power and Orientation*, Elsevier Publishing Company, Inc., Amsterdam, **1946**.

[53] K. R. K. Iyer, P. Neelakantan, T. Radhakrishnan, *J. Polym. Sci. Part A-2 Polym. Phys.* **1968**, *6*, 1747.

[54] B. Frka-Petesic, J. Sugiyama, S. Kimura, H. Chanzy, G. Maret, *Macromolecules* **2015**, *48*, 8844.

[55] E. D. Cranston, D. G. Gray, *Colloids Surfaces A Physicochem. Eng. Asp.* **2008**, *325*, 44.

[56] A. G. Dumanli, H. M. van der Kooij, G. Kamita, E. Reisner, J. J. Baumberg, U. Steiner, S. Vignolini, *ACS Appl. Mater. Interfaces* **2014**, *6*, 12302.

[57] M. S. Reid, M. Villalobos, E. D. Cranston, *Nanoscale* **2016**, *8*, 12247.

[58] R. M. Parker, B. Frka-Petesic, G. Guidetti, G. Kamita, G. Consani, C. Abell, S. Vignolini, *ACS Nano* **2016**, *10*, 8443.

[59] J. N. Israelachvili, *Intermolecular and Surface Forces (Third Edition)*, Academic Press, San Diego, **2011**.

[60] P. A. Buining, A. P. Philipse, H. N. W. Lekkerkerker, *Langmuir* **1994**, *10*, 2106.

[61] X. M. Dong, T. Kimura, J.-F. Revol, D. G. Gray, *Langmuir* **1996**, *12*, 2076.

[62] X. M. Dong, D. G. Gray, *Langmuir* **1997**, *13*, 2404.

[63] J. Araki, M. Wada, S. Kuga, *Langmuir* **2000**, *17*, 21.

[64] E. Lasseuguette, *Cellulose* **2008**, *15*, 571.

[65] E. Kloser, D. G. Gray, *Langmuir* **2010**, *26*, 13450.

[66] F. Azzam, L. Heux, B. Jean, *Langmuir* **2016**, *32*, 4305.

[67] S. Elazzouzi-Hafraoui, J.-L. Putaux, L. Heux, *J. Phys. Chem. B* **2009**, *113*, 11069.

[68] D. Bonn, H. Tanaka, G. Wegdam, H. Kellay, J. Meunier, *Europhys. Lett.* **2007**, *45*, 52.

[69] E. Zaccarelli, *J. Phys. Cond. Mat.* **2007**, *19*, 323101.

[70] M. Nordenström, A. B. Fall, G. Nyström, L. Wågberg, *Langmuir* **2017**, DOI 10.1021/acs.langmuir.7b01832.

[71] T. Phan-Xuan, A. Thuresson, M. Skepö, A. Labrador, R. Bordes, A. Matic, *Cellulose* **2016**, *23*, 3653.

[72] S. Shafiei-Sabet, W. Y. Hamad, S. G. Hatzikiriakos, *Cellulose* **2014**, *21*, 3347.

[73] S. Beck, J. Bouchard, *Nord. Pulp Pap. Res. J.* **2014**, *29*, 6.

[74] L. Onsager, *Ann. N. Y. Acad. Sci.* **1949**, *51*, 627.

[75] S.-D. Lee, *J. Chem. Phys.* **1987**, *87*, 4972.

[76] X. Xiao, P. Sheng, *Phys. Rev. E* **2013**, *88*, 62501.

[77] T. Odijk, *Macromolecules* **1986**, *19*, 2313.

[78] H. H. Wensink, G. J. Vroege, *J. Chem. Phys.* **2003**, *119*, 6868.

[79] A. Stroobants, H. N. W. Lekkerkerker, T. Odijk, *Macromolecules* **1986**, *19*, 2232.

[80] T. Sato, A. Teramoto, *Phys. A Stat. Mech. its Appl.* **1991**, *176*, 72.

[81] M. Khandelwal, A. Windle, *Carbohydr. Polym.* **2014**, *106*, 128.

[82] H. Coles, in *Handb. Liq. Cryst.* (Eds.: D. Demus, J. Goodby, G.W. Gray, H.-W. Spiess, V. Vill), Wiley-VCH Verlag GmbH, **1998**, pp. 335–409.

[83] H. de Vries, *Acta Crystallogr.* **1951**, *4*, 219.

[84] E. I. Kats, *Sov. Phys. JETP* **1971**, *32*, 1004.

[85] R. Nityananda, *Mol. Cryst. Liq. Cryst.* **1973**, *21*, 315.

[86] V. A. Belyakov, V. E. Dmitrienko, V. P. Orlov, *Sov. Phys. Uspekhi* **1979**, *22*, 64.

[87] W. D. St. John, W. J. Fritz, Z. J. Lu, D. K. Yang, *Phys. Rev. E* **1995**, *51*, 1191.

[88] B. D. Wilts, A. G. Dumanli, R. Middleton, P. Vukusic, S. Vignolini, *APL Photonics* **2017**, *2*, 40801.

[89] D. W. Berreman, *J. Opt. Soc. Am.* **1972**, *62*, 502.

[90] R. Dreher, G. Meier, *Phys. Rev. A* **1973**, *8*, 1616.

[91] C. Schütz, M. Agthe, A. B. Fall, K. Gordeyeva, V. Guccini, M. Salajková, T. S.

Plivelic, J. P. F. Lagerwall, G. Salazar-Alvarez, L. Bergström, *Langmuir* **2015**, *31*, 6507.

[92] B. Frka-Petesic, H. Radavidson, B. Jean, L. Heux, *Adv. Mater.* **2017**, *29*, 1606208.

[93] G. H. Conners, *J. Opt. Soc. Am.* **1968**, *58*, 875.

[94] J.-F. Revol, D. L. Godbout, D. G. Gray, *Solidified Liquid Crystals of Cellulose with Optically Variable Properties*, **1997**, US Patent 5,629,055.

[95] J.-F. Revol, D. L. Godbout, D. G. Gray, *J. pulp Pap. Sci.* **1998**, *24*, 146.

[96] Q. Chen, P. Liu, F. Nan, L. Zhou, J. Zhang, *Biomacromolecules* **2014**, *15*, 4343.

[97] J. Pan, W. Hamad, S. K. Straus, *Macromolecules* **2010**, *43*, 3851.

[98] J. H. Park, J. Noh, C. Schütz, G. Salazar-Alvarez, G. Scalia, L. Bergström, J. P. F. Lagerwall, *ChemPhysChem* **2014**, *15*, 1477.

[99] P.-X. Wang, W. Y. Hamad, M. J. MacLachlan, *Nat. Commun.* **2016**, *7*, 11515.

[100] A. G. Dumanli, G. Kamita, J. Landman, H. van der Kooij, B. J. Glover, J. J. Baumberg, U. Steiner, S. Vignolini, *Adv. Opt. Mater.* **2014**, *2*, 646.

[101] S. Elazzouzi, Self-Organization of Cellulose Whiskers Suspended in Water or in Apolar Organic Solvents, Thesis, **2006**.

[102] A. H. Chowdhury, P. S. Russo, *J. Chem. Phys.* **1990**, *92*, 5744.

[103] M. P. B. Van Bruggen, J. K. G. Dhont, H. N. W. Lekkerkerker, *Macromolecules* **1999**, *32*, 2256.

[104] M. S. Reid, S. A. Kedzior, M. Villalobos, E. D. Cranston, *Langmuir* **2017**, *33*, 7403.

[105] J. Majoinen, E. Kontturi, O. Ikkala, D. G. Gray, *Cellulose* **2012**, *19*, 1599.

[106] X. Mu, D. G. Gray, *Langmuir* **2014**, *30*, 9256.

[107] J. L. Fergason, *Mol. Cryst.* **1966**, *1*, 293.

[108] G. Kamita, B. Frka-Petesic, A. Allard, M. Dargaud, K. King, A. G. A. G. Dumanli, S. Vignolini, *Adv. Opt. Mater.* **2016**, *4*, 1950.

[109] B. Frka-Petesic, G. Guidetti, G. Kamita, S. Vignolini, *Adv. Mater.* **2017**, *29*, 1701469.

[110] K. E. Shopsowitz, H. Qi, W. Y. Hamad, M. J. MacLachlan, *Nature* **2010**, *468*, 422.

[111] K. Yao, Q. Meng, V. Bulone, Q. Zhou, *Adv. Mater.* **2017**, 1701323.

[112] M. Giese, M. K. Khan, W. Y. Hamad, M. J. MacLachlan, *ACS Macro Lett.* **2013**, *2*, 818.

[113] A. Hirai, O. Inui, F. Horii, M. Tsuji, *Langmuir* **2009**, *25*, 497.

[114] X. M. Dong, D. G. Gray, *Langmuir* **1997**, *13*, 2404.

[115] J. A. Kelly, K. E. Shopsowitz, J. M. Ahn, W. Y. Hamad, M. J. MacLachlan, *Langmuir* **2012**, *28*, 17256.

[116] F. Jiang, A. R. Esker, M. Roman, *Langmuir* **2010**, *26*, 17919.

[117] S. Dussi, S. Belli, R. Van Roij, M. Dijkstra, *J. Chem. Phys.* **2015**, *142*, 74905.

[118] H. B. Kolli, E. Frezza, G. Cinacchi, A. Ferrarini, A. Giacometti, T. S. Hudson, C. De Michele, F. Sciortino, *Soft Matter* **2014**, *10*, 8171.

[119] S. Beck, J. Bouchard, R. Berry, *Biomacromolecules* **2011**, *12*, 167.

[120] K. J. De France, K. G. Yager, T. Hoare, E. D. Cranston, *Langmuir* **2016**, *32*, 7564.

[121] S. Beck, J. Bouchard, G. Chauve, R. Berry, *Cellulose* **2013**, *20*, 1401.

[122] Y. Nishiyama, S. Kuga, M. Wada, T. Okano, *Macromolecules* **1997**, *30*, 6395.

[123] T. Ebeling, M. Paillet, R. Borsali, O. Diat, A. Dufresne, J. Y. Cavaillé, H. Chanzy, *Langmuir* **1999**, *15*, 6123.

[124] I. Hoeger, O. J. Rojas, K. Efimenko, O. D. Velev, S. S. Kelley, *Soft Matter* **2011**, *7*, 1957.

[125] J. A. Diaz, X. Wu, A. Martini, J. P. Youngblood, R. J. Moon, *Biomacromolecules* **2013**, *14*, 2900.

[126] M. Tatsumi, Y. Teramoto, Y. Nishio, *Cellulose* **2015**, *22*, 2983.

[127] C. D. Edgar, D. G. Gray, *Cellulose* **2003**, *10*, 299.

[128] F. Khelifa, Y. Habibi, P. Leclère, P. Dubois, *Nanoscale* **2013**, *5*, 1082.

[129] R. A. Chowdhury, S. X. Peng, J. Youngblood, *Cellulose* **2017**, *24*, 1957.

[130] L. Csoka, I. C. Hoeger, P. Peralta, I. Peszlen, O. J. Rojas, *J. Colloid Interface Sci.* **2011**, *363*, 206.

[131] M. Ličen, B. Majaron, J. Noh, C. Schütz, L. Bergström, J. Lagerwall, I. Drevenšek-Olenik, *Cellulose* **2016**, *23*, 3601.

[132] D. Bordel, J. L. Putaux, L. Heux, *Langmuir* **2006**, *22*, 4899.

[133] Y. Habibi, T. Heim, R. Douillard, *J. Polym. Sci. Part B Polym. Phys.* **2008**, *46*, 1430.

[134] B. Frka-Petesic, B. Jean, L. Heux, *EPL* **2014**, *107*, 28006.

[135] H. Oulachgar, M. Bolduc, G. Chauve, Y. Desroches, P. Beaupre, J. Bouchard, P. Galarneau, *MRS Adv.* **2015**, *1*, 631.

[136] J. Sugiyama, H. Chanzy, G. Maret, *Macromolecules* **1992**, *25*, 4232.

[137] J.-F. Revol, L. Godbout, X.-M. Dong, D. G. Gray, H. Chanzy, G. Maret, *Liq. Cryst.* **1994**, *16*, 127.

[138] F. Kimura, T. Kimura, M. Tamura, A. Hirai, M. Ikuno, F. Horii, *Langmuir* **2005**, *21*, 2034.

[139] F. Kimura, T. Kimura, *Sci. Technol. Adv. Mater.* **2008**, *9*, 24212.

[140] M. Tatsumi, F. Kimura, T. Kimura, Y. Teramoto, Y. Nishio, *Biomacromolecules* **2014**, *15*, 4579.

[141] G. Song, F. Kimura, T. Kimura, G. Piao, *Macromolecules* **2013**, *46*, 8957.

[142] C. D. Edgar, D. G. Gray, *Cellulose* **2001**, *8*, 5.

[143] T. Pullawan, A. N. Wilkinson, S. J. Eichhorn, *J. Mater. Sci.* **2013**, *48*, 7847.

[144] M. Roman, D. G. Gray, *Langmuir* **2005**, *21*, 5555.

[145] T. Hiratani, W. Y. Hamad, M. J. MacLachlan, *Adv. Mater.* **2017**, *29*, 1606083.

[146] M. Urbanski, C. G. Reyes, J. Noh, A. Sharma, Y. Geng, V. Subba Rao Jampani, J. P. F. Lagerwall, *J. Phys. Condens. Matter* **2017**, *29*, 133003.

[147] Z. S. Davidson, Y. Huang, A. Gross, A. Martinez, T. Still, C. Zhou, P. J. Collings, R. D. Kamien, A. G. Yodh, *Nat. Commun.* **2017**, *8*, 15642.

[148] V. A. Lubarda, K. A. Talke, *Langmuir* **2011**, *27*, 10705.

[149] X. Mu, D. G. Gray, *Cellulose* **2015**, *22*, 1103.

[150] L. Cui, J. Zhang, X. Zhang, L. Huang, Z. Wang, Y. Li, H. Gao, S. Zhu, T. Wang, B. Yang, *ACS Appl. Mater. Interfaces* **2012**, *4*, 2775.

[151] A. Gençer, C. Schütz, W. Thielemans, *Langmuir* **2017**, *33*, 228.

[152] A. Crivoi, F. Duan, *Langmuir* **2013**, *29*, 12067.

[153] M. Anyfantakis, Z. Geng, M. Morel, S. Rudiuk, D. Baigl, *Langmuir* **2015**, *31*, 4113.

[154] M. Anyfantakis, D. Baigl, *ChemPhysChem* **2015**, *16*, 2726.

[155] M. Roman, F. Navarro, in *Model Cellul. Surfaces*, American Chemical Society, **2009**, pp. 157–171.

[156] D. G. Gray, X. Mu, *Materials* **2015**, *8*, 7873.

[157] N. J. Cira, A. Benusiglio, M. Prakash, *Nature* **2015**, *519*, 446.

[158] Y. Li, J. Jun-Yan Suen, E. Prince, E. M. Larin, A. Klinkova, H. Thérien-Aubin, S. Zhu, B. Yang, A. S. Helmy, O. D. Lavrentovich, E. Kumacheva, *Nat. Commun.* **2016**, *7*, 12520.

[159] C. Robinson, J. C. Ward, R. B. Beevers, *Discuss. Faraday Soc.* **1958**, *25*, 29.

[160] F. Xu, P. Crooker, *Phys. Rev. E* **1997**, *56*, 6853.

[161] J. Bezić, S. Žumer, *Liq. Cryst.* **1992**, *11*, 593.

[162] Y. Li, E. Prince, S. Cho, A. Salari, Y. Mosaddeghian Golestani, O. D. Lavrentovich, E. Kumacheva, *Proc. Natl. Acad. Sci. U. S. A.* **2017**, *114*, 2137.

[163] P. X. Wang, W. Y. Hamad, M. J. MacLachlan, *Angew. Chemie Int. Ed.* **2016**, *55*, 12460.

[164] S. Cho, Y. Li, M. Seo, E. Kumacheva, *Angew. Chemie Int. Ed.* **2016**, *55*, 14014.

[165] C. Honorato-Rios, A. Kuhnhold, J. R. Bruckner, R. Dannert, T. Schilling, J. P. F. Lagerwall, *Front. Mater.* **2016**, *3*, 21.

[166] G. Guidetti, S. Atifi, S. Vignolini, W. Y. Hamad, *Adv. Mater.* **2016**, *28*, 10042.

[167] R. Bardet, N. Belgacem, J. Bras, *ACS Appl. Mater. Interfaces* **2015**, *7*, 4010.

[168] B. Zhu, R. Merindol, A. J. Benitez, B. Wang, A. Walther, *ACS Appl. Mater. Interfaces* **2016**, *8*, 11031.

[169] M. Gu, C. Jiang, D. Liu, N. Prempeh, I. I. Smalyukh, *ACS Appl. Mater. Interfaces* **2016**, *8*, 32565.

[170] B. Vollick, P.-Y. Kuo, H. Thérien-Aubin, N. Yan, E. Kumacheva, *Chem. Mater.* **2017**, *29*, 789.

[171] M. Schlesinger, M. Giese, L. K. Blusch, W. Y. Hamad, M. J. MacLachlan, *Chem. Commun.* **2015**, *51*, 530.

[172] A. Querejeta-Fernández, G. Chauve, M. Methot, J. Bouchard, E. Kumacheva, *J. Am. Chem. Soc.* **2014**, *136*, 4788.

[173] A. Querejeta-Fernández, B. Kopera, K. S. Prado, A. Klinkova, M. Methot, G. Chauve, J. Bouchard, A. S. Helmy, E. Kumacheva, *ACS Nano* **2015**, *9*, 10377.

[174] A. Lukach, H. Thérien-Aubin, A. Querejeta-Fernández, N. Pitch, G. Chauve, M. Méthot, J. Bouchard, E. Kumacheva, *Langmuir* **2015**, *31*, 5033.

[175] T.-D. Nguyen, W. Y. Hamad, M. J. MacLachlan, *Adv. Opt. Mater.* **2017**, *5*, 1600514.

[176] E. Lizundia, T.-D. Nguyen, J. L. Vilas, W. Y. Hamad, M. J. MacLachlan, *Mater. Chem. Front.* **2017**, *1*, 979.

[177] R. Bardet, F. Roussel, S. Coindeau, N. Belgacem, J. Bras, *Carbohydr. Polym.* **2015**, *122*, 367.

[178] F. Nan, S. Nagarajan, Y. Chen, P. Liu, Y. Duan, Y. Men, J. Zhang, *ACS Sustain. Chem. Eng.* **2017**, acssuschemeng.7b01749.

[179] J. A. Kelly, M. Giese, K. E. Shopsowitz, W. Y. Hamad, M. J. MacLachlan, *Acc. Chem. Res.* **2014**, *47*, 1088.

[180] M. K. Khan, A. Bsoul, K. Walus, W. Y. Hamad, M. J. Maclachlan, *Angew. Chemie Int. Ed.* **2015**, *54*, 4304.

[181] A. Espinha, G. Guidetti, M. C. Serrano, B. Frka-Petesic, A. G. Dumanli, W. Y. Hamad, Á. Blanco, C. López, S. Vignolini, *ACS Appl. Mater. Interfaces* **2016**, *8*, 31935.

[182] T. Wu, J. Li, J. Li, S. Ye, J. Wei, J. Guo, *J. Mater. Chem. C* **2016**, *4*, 9687.

[183] S. N. Fernandes, P. L. Almeida, N. Monge, L. E. Aguirre, D. Reis, C. L. P. de Oliveira, A. M. F. Neto, P. Pieranski, M. H. Godinho, *Adv. Mater.* **2017**, *29*, 1603560.

[184] J. A. Kelly, A. M. Shukaliak, C. C. Y. Cheung, K. E. Shopsowitz, W. Y. Hamad, M. J. MacLachlan, *Angew. Chemie Int. Ed.* **2013**, *52*, 8912.

[185] Y. P. Zhang, V. P. Chodavarapu, A. G. Kirk, M. P. Andrews, *J. Nanophotonics* **2012**, *6*, 63516.

[186] M. Giese, L. K. Blusch, M. K. Khan, W. Y. Hamad, M. J. MacLachlan, *Angew. Chemie Int. Ed.* **2014**, *53*, 8880.

[187] Y. P. Zhang, V. P. Chodavarapu, A. G. Kirk, M. P. Andrews, *Sensors Actuators, B Chem.* **2013**, *176*, 692.

[188] T. Lu, H. Pan, J. Ma, Y. Li, S. W. Bokhari, X. Jiang, S. Zhu, D. Zhang, *ACS Appl. Mater. Interfaces* **2017**, *9*, 18231.

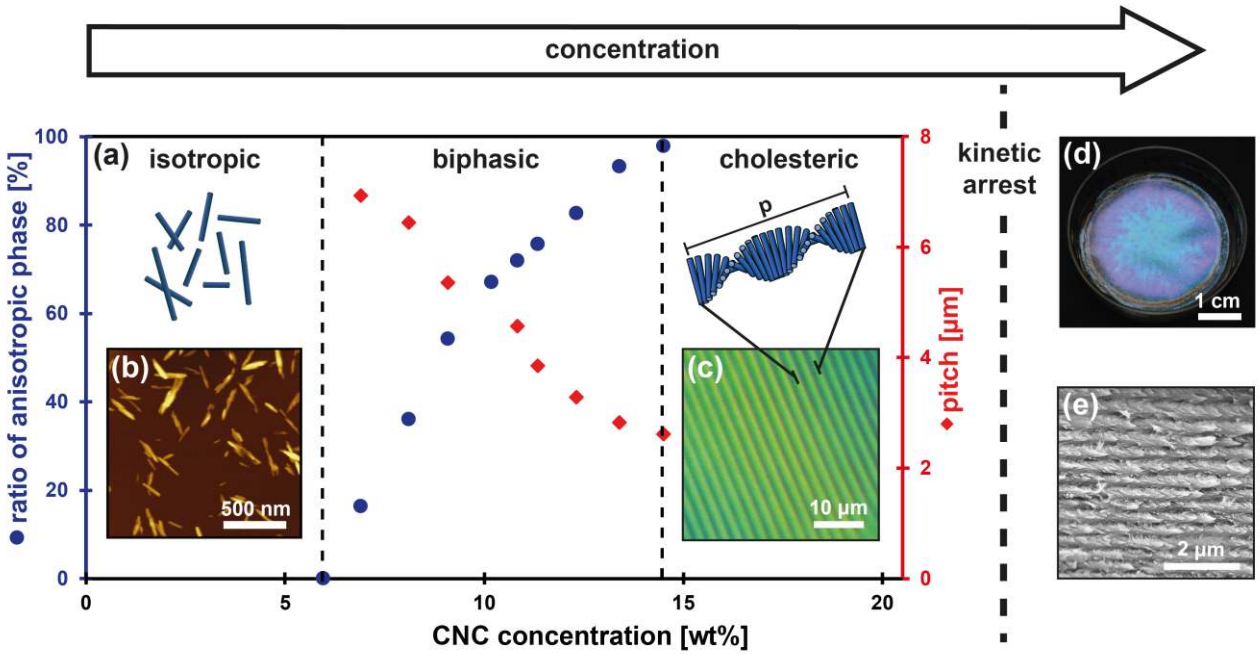

Figure 1. Schematic of the self-assembly of a CNC suspension upon evaporation to form a structurally colored film: **(a)** Phase diagram showing the transition from isotropic to cholesteric phase (*blue dots*) upon increasing CNC concentration and the corresponding equilibrium pitch (*red diamonds*). **(b)** Atomic force micrograph of individual cellulose nanocrystals. **(c)** Polarized optical micrograph of a typical fingerprint pattern of the cholesteric phase. (a-c) Adapted under the terms of the CC-BY license.[58] Copyright 2016, American Chemical Society. **(d)** Photograph of a blue film and **(e)** the corresponding SEM cross section showing the characteristic Bouligand arches. (d-e) Adapted with permission.[109] Copyright 2017, John Wiley and Sons.

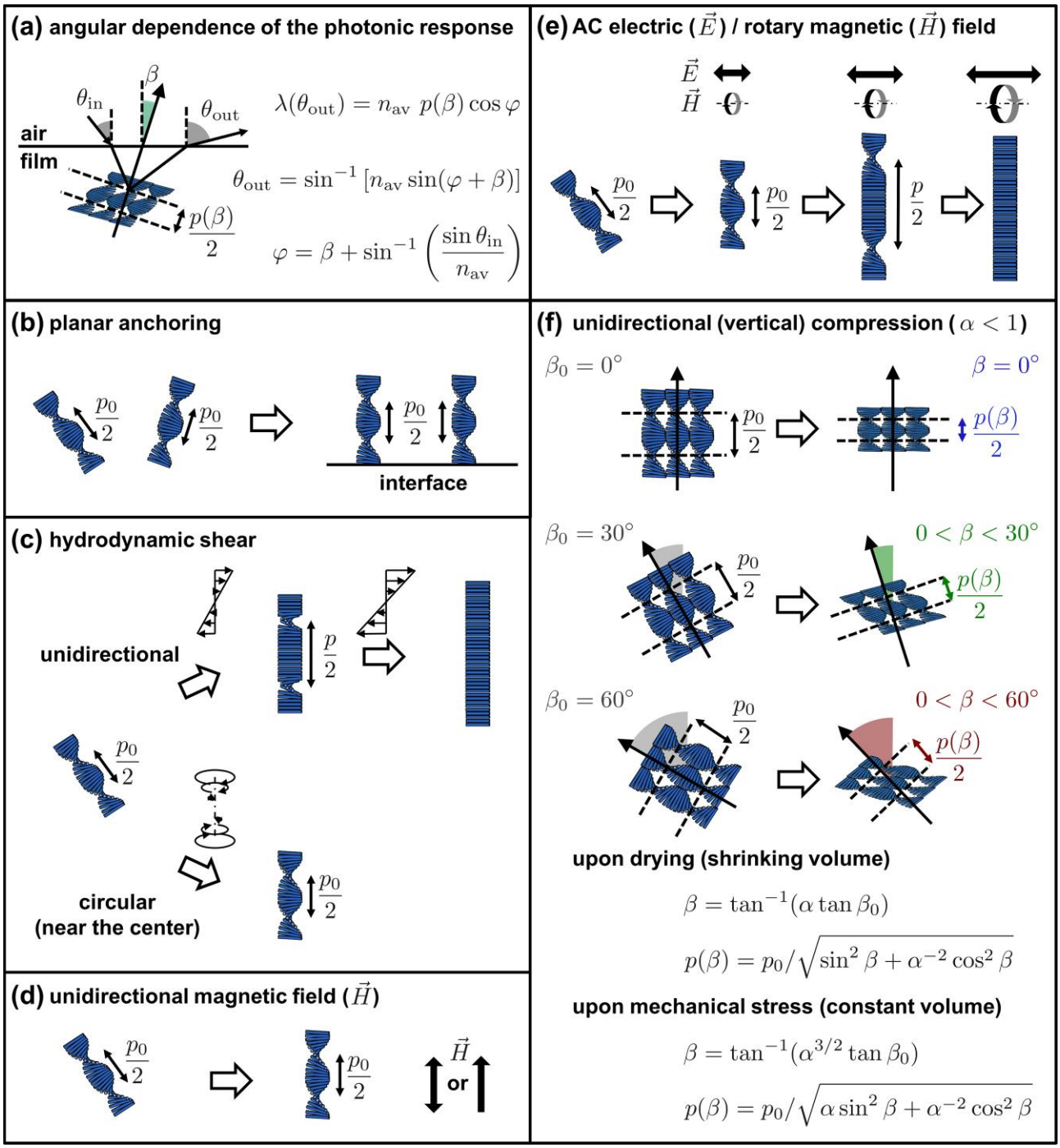

Figure 2. Schematic of the techniques available to control the alignment of cholesteric CNC in suspension and upon drying to give a film: **(a)** A summary of Fergason's law, describing the interaction of light with tilted cholesteric domains. **(b)** Planar anchoring induces a vertical alignment of CNC helicoids with the helical axes perpendicular to the substrate. **(c)** Unidirectional high shear untwists the helicoid, whereas circular shear induces uniform vertical alignment of the axis perpendicular to the substrate. **(d)** Unidirectional magnetic field promotes alignment of the helical axis parallel to the field **(e)** An AC electric field or rotating magnetic field induces alignment, followed by an untwisting of the helix. **(f)** Mechanical compression causes contraction and distortion of the helicoid as a function of the tilt angle of the helical axis with respect to the compression direction.

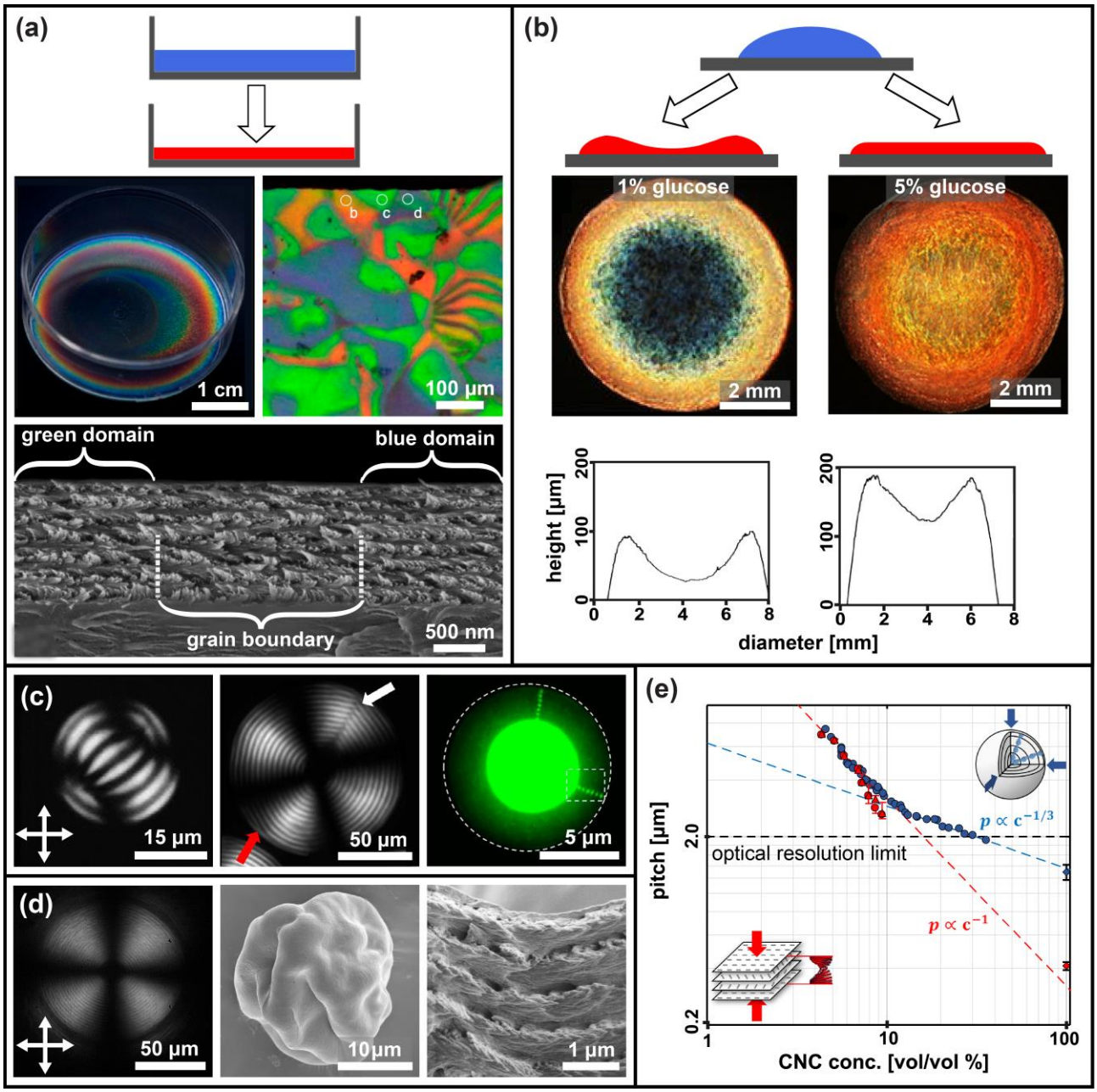

Figure 3. The effect of Geometrical confinement: **(a)** Schematic of a CNC suspension drying in a Petri dish (*top*) and photograph of a very thin CNC film, with corresponding polarized optical microscopy, showing a multidomain structure reflecting left handed circularly polarized light (*middle*). The corresponding SEM cross-section, showing a green domain and a blue domain separated by a grain boundary, is given *below*. Adapted under the terms of the CC-BY license.[56] Copyright 2014, American Chemical Society. **(b)** Schematic depicting a sessile drop of CNC suspension, that upon evaporation can form a coffee ring stain (*left*) or a more uniform film (*right*). The coffee ring effect can be suppressed by addition of a non-volatile additive, e.g. glucose, as shown in the right-hand photograph and profile. Adapted with permission.[149] Copyright 2015, Springer Netherlands. **(c)** Polarized optical micrographs of a small CNC droplet showing a central tactoid surrounded by a Frank-Pryce shell (*left*); in contrast, larger droplets form a radial Frank-Pryce structure, appearing as concentric fingerprints superimposed with a Maltese cross (*center*), containing a central isotropic defect, with further defects (white arrow) and disclinations (red arrow). The disclinations and central defect can accommodate 184 nm nanoparticles, as shown by fluorescence microscopy (*right*).

Adapted under the terms of the CC-BY license.[158] Copyright 2016, Nature Publishing Group. Adapted with permission.[162] Copyright 2017, National Academy of Sciences. **(d)** Polarized optical micrograph of a droplet with a radial Frank-Pryce structure (*left*), that upon evaporation forms a solid, buckled microparticle (*center*) that retains the helicoidal architecture, as shown by SEM cross section. **(e)** Graph showing the dependence of the cholesteric pitch upon CNC concentration for a spherical droplet (*blue dots*) and in comparison, for the film geometry (*red dots*). The point of kinetic arrest and the subsequent effect of the geometry upon compression is clearly observed. (d-e) Adapted under the terms of the CC-BY license.[58] Copyright 2016, American Chemical Society.

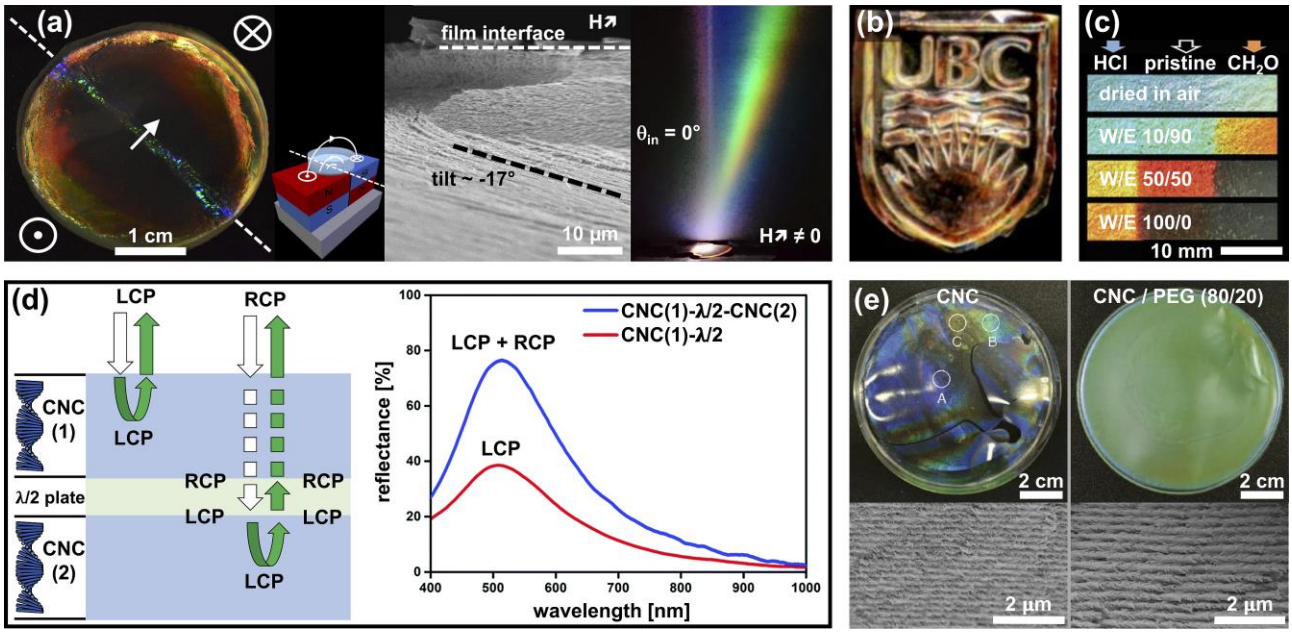

Figure 4. Examples of functional CNC-based materials: **(a)** Control of the CNC helix orientation by exposing the drying CNC suspension to a magnet. The interesting patterns in the colored film (*left*) arise from the magnetically-aligned tilted helices (*center*) and this produces off-specular colors (*right*). Adapted with permission.[109] Copyright 2017, John Wiley and Sons. **(b)** A composite CNC film natively reflects in the infrared, but upon localized compression, an induced blue shift leads to reveal of the design. Adapted with permission.[112] Copyright 2013, American Chemical Society. **(c)** Mesoporous resin films change color in water/ethanol mixtures, with the color change dependent on the pre-treatment of the film. Adapted with permission.[180] Copyright 2015, John Wiley and Sons. **(d)** A schematic of a hyper-reflective structure, produced by sandwiching a λ/2 plate retarder between two layers of CNC (*left*) and the corresponding reflected spectra (*right*). Left circular polarized (LCP) light is reflected by CNC(1), while right circular polarized light (RCP) is transmitted and converted to LCP by the λ/2 plate retarder. This can now be reflected by CNC(2) and passed back to the surface *via* the same mechanism. By interacting with all the incident light, the intensity of the reflected light is effectively double compared to a single CNC film on a λ/2 plate retarder. Adapted with permission.[182] Copyright 2016, Royal Society of Chemistry. **(e)** Comparison between a CNC film (*left*) and a CNC/polyethylene glycol (PEG) composite (*right*) with corresponding SEM cross sections, showing improved color homogeneity and reduced brittleness. Adapted with permission.[111] Copyright 2017, John Wiley and Sons.